

Electronic structures and topological phases of magnetic layered materials MnBi_2Te_4 , MnBi_2Se_4 and MnSb_2Te_4

Ping Li,^{1,*} Jiangying Yu,¹ Ying Wang,¹ and Weidong Luo^{2,3,†}

¹*Key Laboratory of Advanced Electronic Materials and Devices,
School of Physics and Mathematics,
Anhui Jianzhu University, Hefei 230601, China*

²*Key Laboratory of Artificial Structures and Quantum Control,
School of Physics and Astronomy, Shanghai Jiao Tong University, Shanghai 200240, China*

³*Institute of Natural Sciences, Shanghai Jiao Tong University, Shanghai 200240, China*

(Dated: March 8, 2021)

Abstract

First-principles calculations are performed to study the electronic structures and topological phases of magnetic layered materials MnBi_2Te_4 , MnBi_2Se_4 and MnSb_2Te_4 under different film thicknesses, strains and spin-orbit coupling (SOC) strengths. All these compounds energetically prefer the antiferromagnetic (AFM) state. MnBi_2Te_4 and MnSb_2Te_4 bulks are AFM topological insulators (TIs) in the AFM state, while they become Weyl semimetals in the ferromagnetic (FM) state. MnBi_2Se_4 is trivially insulating in both the AFM and FM states, but it becomes an AFM TI or a Weyl semimetal with increasing SOC strength or applying compressive strains. Under equilibrium lattice constants, the FM MnBi_2Te_4 slabs thicker than two septuple layers (SLs), the AFM MnBi_2Te_4 slabs thicker than three SLs and the FM MnSb_2Te_4 slabs thicker than five SLs are all Chern insulators. In addition, Chern insulators can also be obtained by compressing the in-plane lattice constants of the FM MnBi_2Se_4 slabs thicker than four SLs and the FM MnSb_2Te_4 slabs of three or four SLs, but cannot be obtained using the same method in the AFM slabs of these two materials. In-plane tensile strains about 1% to 2% turn the Chern insulators into trivial insulators.

I. INTRODUCTION

The interplay between topological insulators (TIs) and magnetism is frequently used to create topological quantum materials such as Chern insulators, axion insulators and Weyl semimetals¹⁻⁸. These topological phases enable the quantum anomalous Hall (QAH) effect, the topological magnetoelectric (TME) effect and chiral Majorana fermions; and they have potential applications in spintronics and topological quantum computation. Two methods are traditionally used to combine magnetism with TIs, i.e., doping magnetic atoms into TIs⁹⁻¹¹ and constructing TI/magnet heterostructures¹²⁻¹⁴. The former tends to introduce inhomogeneity to the doped bulk, while the latter usually suffers from interfacial band bending¹³. Hence, the obtained systems are usually far from satisfactory.

Very recently, MnBi_2Te_4 has drawn tremendous attention^{2-7,15,16}. This compound is van der Waals (vdW) layered and intrinsically magnetic. Hence, it naturally avoids both the bulk inhomogeneity and the interfacial band bending problems. Three-dimensional (3D) MnBi_2Te_4 shows rich topological phases, and in its ground state it is an antiferromagnetic (AFM) TI^{3,4,6}. The QAH effect has been experimentally observed in MnBi_2Te_4 films^{2,4}, so has the Chern insulator-axion insulator phase transition⁴. Belonging to the same family of materials, MnBi_2Se_4 ¹⁷ and MnSb_2Te_4 ^{18,19} bulks were also investigated and different topological phases were predicted under various conditions. However, these predictions are waiting for experimental tests.

The MnBi_2Te_4 family compounds have small energy gaps^{6,17,19}. Their band structures and hence the topological phases strongly depend on the film thicknesses⁷ and applied strains, which must be carefully considered in experiment. The present work studies the dependence of MnBi_2Te_4 , MnBi_2Se_4 and MnSb_2Te_4 in detail. First-principles calculations are performed to calculate the electronic structures and topological phases of these materials under varying strains and different film thicknesses. The Z_2 invariant and the Chern number C are calculated to identify the TIs and Chern insulators, respectively. Special attention is paid to the QAH systems. The chiral edge states and the quantized Hall conductivity σ_{xy} of the Chern insulators and the Fermi arcs of the Weyl semimetals are presented. These results are of significance to the experimental growth and topological-phase control of the MnBi_2Te_4 family materials.

II. METHOD

First-principles calculations are performed within the density functional theory (DFT) framework as implemented in the VASP codes²⁰. The Mn $3d$ orbital is treated by the generalized gradient approximation²¹ plus Hubbard U (GGA+ U) method with $U = 4.0$ eV. The energy cutoff is 350 eV, and $14 \times 14 \times 2$, $14 \times 14 \times 4$ and $9 \times 9 \times 1$ Monkhorst-Pack K-meshes are used for the calculations of the AFM bulks, the FM bulks and the 2D slabs, respectively. The vdW correction of the optB88-vdW scheme²² is involved to optimize the crystal structures until the force acting on each ion is less than 0.002 eV/Å. For slabs of different thicknesses, a vacuum of 18 Å is introduced to minimize the image-image interactions due to the periodic boundary condition. The electronic properties of the AFM and FM MnBi_2Te_4 bulks are confirmed by the HSE06 hybrid functional calculations^{23,24}, and qualitatively consistent results are obtained. Topological invariants, surface and edge states are calculated based on the maximally localized Wannier functions using the WannierTools package²⁵.

III. RESULTS

MnBi_2Te_4 , MnBi_2Se_4 and MnSb_2Te_4 crystallize in the same rhombohedral structure with the $R\bar{3}m$ space group. We take MnBi_2Te_4 as an example and show its structure in Fig. 1. It consists of Te-Bi-Te-Mn-Te-Bi-Te septuple layers (SLs) stacking along the c axis through the vdW interaction. The calculated lattice constants and the energy differences $\Delta E = E(\text{FM}) - E(\text{AFM})$ between the FM and the respective AFM phases are listed in Table I, accompanied with previously reported calculation and experimental data^{6,17,19}. The current data agrees well with the previous reports. The energy differences ΔE are all positive, indicating that the AFM state is energetically more favorable, also in agreement with previous studies^{6,17,19}.

A. AFM MnBi_2Te_4 , MnBi_2Se_4 and MnSb_2Te_4 bulks

Figures 2 (a), (b) and (c) show the calculated band structures of AFM MnBi_2Te_4 , MnBi_2Se_4 and MnSb_2Te_4 bulks, respectively. From the figures, the three crystals are all insulating. Both the valence band maxima (VBMs) and the conduction band minima (CBMs) are located at the Γ point, forming direct energy gaps of 138, 140 and 16 meV, respectively.

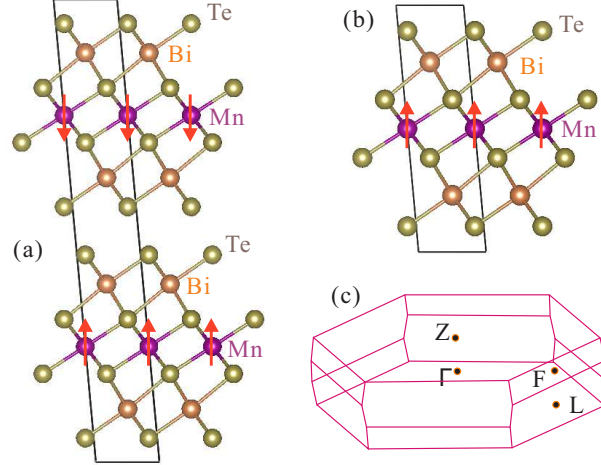


FIG. 1. Crystal structures of (a) AFM and (b) FM MnBi_2Te_4 , where the arrows indicate the directions of the magnetic moments. (c) Brillouin zone of the crystals.

Li *et al.*⁶ predicted energy gaps of about 0.16 and 0.18 eV at the Z and Γ points in AFM MnBi_2Te_4 , respectively. Γ -point direct energy gaps were also theoretically reported in AFM MnBi_2Se_4 ¹⁷ and MnSb_2Te_4 ¹⁹. In experiment the measured energy gap of AFM MnBi_2Se_4 by electrical transport is 0.15 eV²⁶, in very good agreement with our data. Figs. 2 (a) and (c) show that the energy bands of AFM MnBi_2Te_4 and MnSb_2Te_4 are inverted around the Γ point near the Fermi level, while the inversion does not occur in the bands of AFM MnBi_2Se_4 as Fig. 2 (b) shows. The band-inversion features agree with the previous reports in the MnBi_2Te_4 case⁶ but disagree with the reports in MnBi_2Se_4 and MnSb_2Te_4 cases^{17,19}. We attribute the disagreement to the differences of atomic geometries or lattice constants used or obtained in calculations (see Table I).

Band inversion usually means topologically nontrivial materials, such as 3D TIs^{6,19,27} and quantum spin Hall (QSH) insulators²⁸. The MnBi_2Te_4 family AFM compounds lose both the time-reversal symmetry (Θ) and the primitive-lattice translational symmetry ($T_{1/2}$) but preserves the combination $S = \Theta T_{1/2}$. Hence, they can be classified according to the Z_2 invariant⁸. To determine their topological nature, the Wannier charge centers (WCCs) are calculated. Figs. 2 (d) and (e) show the evolution of WCCs in the $k_z = 0$ plane of MnBi_2Te_4 and MnBi_2Se_4 , respectively. That of AFM MnSb_2Te_4 is similar to Fig. 2 (d), thus it is not shown here. Fig. 2 (d) indicates the topological invariant $Z_2 = 1$ for AFM MnBi_2Te_4 , i.e., it is an AFM TI, so is AFM MnSb_2Te_4 . Fig. 2 (e) gives a topological

TABLE I. Lattice constants of MnBi_2Te_4 family materials and the energy differences $\Delta E = E(\text{FM}) - E(\text{AFM})$ between the FM phases and the respective AFM phases. Here, the available data in previous theoretical or experimental reports is presented for comparison.

		MnBi_2Te_4	MnBi_2Se_4	MnSb_2Te_4
a (Å)	This work	4.346	4.085	4.281
	Other calc.	4.36 ⁶	4.29, 4.22 ¹⁷	-
		4.45, 4.37 ¹⁷		
	Expt. data	4.334 ¹⁷	4.197 ¹⁷	4.2385, 4.2219 ¹⁸ 4.2613 ¹⁹
c (Å)	This work	41.145	38.551	40.510
	Other calc.	40.6 ⁶	38.94, 38.52 ¹⁷	-
		41.82, 41.38 ¹⁷		
	Expt. data	40.91 ¹⁷	37.797 ¹⁷	40.8497, 40.606 ¹⁸ 41.062 ¹⁹
$\Delta E(\text{meV}/\text{Mn})$	This work	0.3	0.6	1.0
	Other calc.	1.2 ⁶	1.5 ¹⁷	-

invariant $Z_2 = 0$, thus AFM MnBi_2Se_4 is trivial. The calculated topological invariants are consistent with the band-inversion features illustrated in Figs. 2 (a) to (c). Different groups have predicted MnBi_2Te_4 as an AFM TI^{3,6}, in agreement with the current results. While AFM MnBi_2Se_4 and MnSb_2Te_4 bulks were predicted to be topologically nontrivial and trivial^{17,19}, respectively. These differences can be also explained in terms of the differences of lattice constants. According to the calculations by Zhou *et al.*¹⁹, when c is decreased by 6%, AFM MnSb_2Te_4 also becomes an AFM TI. The common mechanism of TIs is the spin-orbit coupling (SOC) induced band inversion^{29,30}. The heavy atoms in MnBi_2Te_4 produce the strong SOC and a large inverted energy gap of 138 meV. The Sb atom is lighter than the Bi atom, so the SOC is weaker in MnSb_2Te_4 , resulting in an inverted energy gap of only 16 meV. This gap is so small that the topological phase of AFM MnSb_2Te_4 can be easily changed by external perturbations, such as tensile strains. The SOC of the Se atom is also weaker than that of the Te atom, so that band inversion cannot occur in AFM MnBi_2Se_4 , leading to a trivial state.

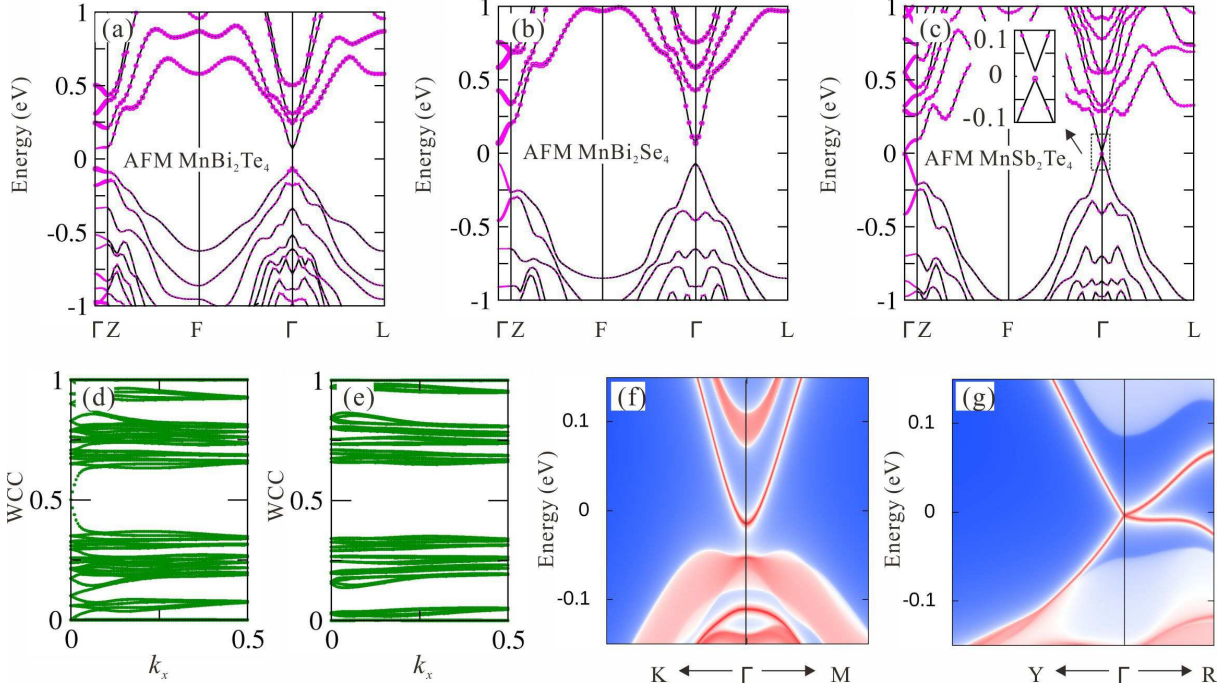


FIG. 2. Band structures of AFM (a) MnBi_2Te_4 , (b) MnBi_2Se_4 and (c) MnSb_2Te_4 , where the magenta symbols denote the Bi- p or the Sb- p projections, and the symbol size indicates the contribution weight. Evolution of WCCs of AFM (d) MnBi_2Te_4 and (e) MnBi_2Se_4 in the $k_z = 0$ plane. Surface states of AFM MnBi_2Te_4 in (f) (001) and (g) (101) surfaces.

In theory, AFM TIs are metallic along some surfaces but insulating along others to support the half-quantum Hall effect with $\sigma_{xy} = e^2/(2h)^8$. This is different from strong TIs, which have gapless Dirac surface states along all the surfaces^{29,30}. Figs. 2 (f) and (g) show the calculated surface states of AFM MnBi_2Te_4 along the (001) and (101) surfaces, respectively. The former is obviously gapped while the latter exhibits gapless surface states, in consistent with the theory⁸. Moreover, energy distribution curves (EDC) recently resolved an energy gap of about 70 meV at the surface states of the (001) surface of AFM MnBi_2Te_4 ³, also in agreement with our results.

The electronic structures and consequently the topological phases of materials are closely related to applied strains^{27,28}. Fig. 3 (a) shows the energy gaps and topological phases of AFM MnBi_2Te_4 , MnBi_2Se_4 and MnSb_2Te_4 at different strains. Here the isotropic strain is evaluated by

$$\epsilon = 100 \times (a - a_0)\%, \quad (1)$$

where a and a_0 are the strained and unstrained lattice constants, respectively. According to Eq. (1), a negative ϵ indicates a compressive strain, while a positive ϵ means a tensile strain.

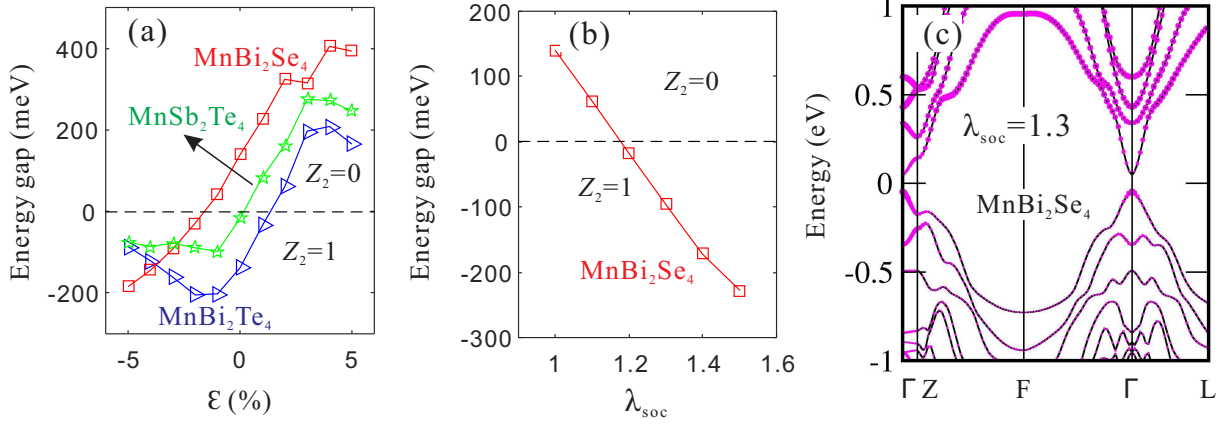


FIG. 3. (a) Energy gaps and topological phases of AFM MnBi₂Te₄, MnBi₂Se₄ and MnSb₂Te₄ at different strains. (b) Evolution of topological phase and energy gaps of AFM MnBi₂Se₄ following the SOC strength λ_{soc} . Positive and negative energy gaps mean that the bulks are trivial insulators with $Z_2 = 0$ and AFM TIs with $Z_2 = 1$, respectively, and the absolute values of the gaps correspond to the gap sizes. (c) Band structure of AFM MnBi₂Se₄ at $\lambda_{\text{soc}} = 1.3$.

Figure 3 (a) shows that around the equilibrium lattice constants, the topological phases of the three AFM bulks are very sensitive to applied strains. Under small compressive strains, the energy gaps of AFM MnBi₂Te₄ and MnSb₂Te₄ quickly increase but the two bulks remain as AFM TIs. The energy gap of AFM MnBi₂Te₄ reaches the largest value of 204 meV at $\epsilon = -2\%$. That of AFM MnSb₂Te₄ rapidly arrives at the maximum of 98 meV at a small compressive strain $\epsilon = -1\%$ from its equilibrium value of 16 meV. Further compressing the bulks, the energy gaps will decrease, but the nontrivial phase can be kept at least for $\epsilon \geq -5\%$. At equilibrium lattice constants, AFM MnBi₂Se₄ is trivial. From Fig. 3 (a), it can be turned into an AFM TI by small or moderate compressive strains. Between $\epsilon = -1\%$ and -2% the energy gap closes and reopens, and AFM MnBi₂Se₄ transits from the trivial phase with $Z_2 = 0$ to the nontrivial phase with $Z_2 = 1$. It becomes an AFM TI. The nontrivial energy gap at $\epsilon = -2\%$ is 29 meV, which rapidly increases to 184 meV at $\epsilon = -5\%$. On the other hand, tensile strains turn the AFM bulks from the nontrivial phase into the trivial phase. A tensile strain less than 1% is able to turn AFM MnSb₂Te₄ to be a trivial insulator

because of its rather small equilibrium energy gap (16 meV). At tensile strains around 1%, AFM MnBi₂Te₄ keeps in the nontrivial phase. However, at $\epsilon = 2\%$ it becomes a trivial insulator with an energy gap of 62 meV.

The SOC strength λ_{soc} of AFM MnBi₂Se₄ is adjusted, and the energy-gap evolution is shown in Fig. 3 (b). In this work, λ_{soc} is referenced with respect to the original value. For example, $\lambda_{\text{soc}} = 1.1$ means the SOC strength is adjusted to 1.1 times of the original value. At $\lambda_{\text{soc}} = 1.0$, the bulk is in a trivial state with $Z_2 = 0$ and an energy gap of 140 meV. As λ_{soc} increases, the energy gap linearly decreases. It closes and reopens near $\lambda_{\text{soc}} = 1.2$, and phase transition occurs. The compound evolves into a nontrivial state with $Z_2 = 1$, corresponding to an AFM TI. The phase transition is accompanied by band inversion. Fig. 3 (c) shows the band structure of AFM MnBi₂Se₄ with $\lambda_{\text{soc}} = 1.3$. Comparing Fig. 3 (c) with Fig. 2 (b), band inversion can be clearly resolved around the Γ point near the Fermi level.

B. FM MnBi₂Te₄, MnBi₂Se₄ and MnSb₂Te₄ bulks

The energy differences ΔE between the AFM and the FM states are very small for the considered bulks (see Table I), rendering it possible to artificially tune the materials from the AFM state to the FM state. In experiment, such a magnetic phase transition has recently been observed in 6 SLs MnBi₂Te₄ slabs at a critical magnetic field $\mu_0 H_c = 4.55 \text{ T}^4$.

Figures 4 (a), (b) and (c) show the calculated energy band structures of FM MnBi₂Te₄, MnBi₂Se₄ and MnSb₂Te₄, respectively. From the figures FM MnBi₂Te₄ and MnSb₂Te₄ are Weyl semimetals. They each have a pair of Weyl points W and W', which are located on the $-\text{Z}-\Gamma-\text{Z}$ line and symmetrical about the Γ point. The Weyl points of FM MnBi₂Te₄ appear at $k_z = \pm 0.012 \text{ \AA}^{-1}$, and those of FM MnSb₂Te₄ are at $k_z = \pm 0.021 \text{ \AA}^{-1}$. To see clearly the Weyl points and the Weyl cones, for instance, we show the energy dispersion of FM MnSb₂Te₄ in the k_x-k_z plane in Fig. 4 (d). According to the WCC calculations, the Weyl chirality of the W point is +1, as Fig. 4 (e) shows by taking FM MnSb₂Te₄ as an example, while that of the W' point is -1. The present results show that FM MnBi₂Te₄ is a type-II Weyl semimetal, in agreement with previous calculations⁶, while FM MnSb₂Te₄ is a type-I Weyl semimetal. We note that previous reports on FM MnSb₂Te₄ are different. Zhou *et al.*¹⁹ predicted an energy gap of 7.75 meV in FM MnSb₂Te₄, while Murakami *et al.*¹⁸ predicted it as a type-II Weyl semimetal. Once again we attribute these differences to the

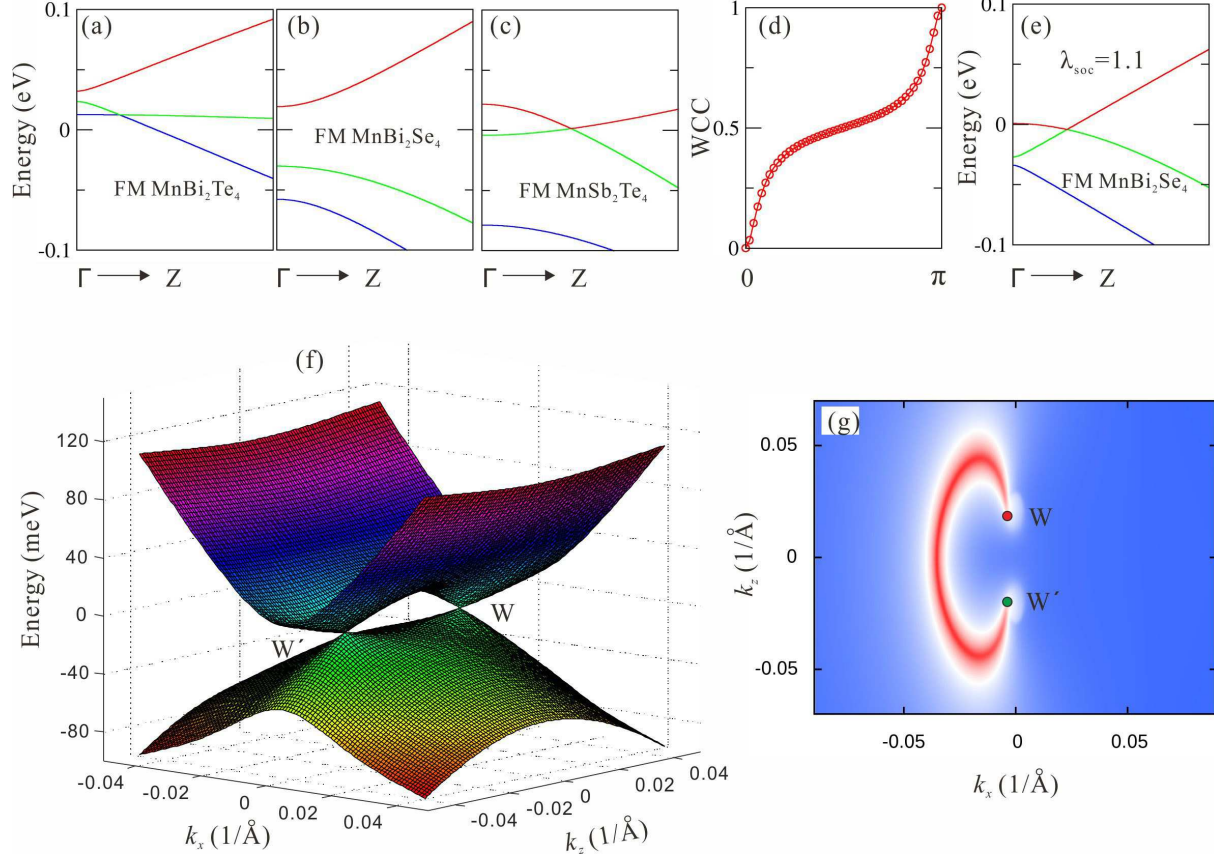


FIG. 4. Band structures of FM (a) MnBi_2Te_4 , (b) MnBi_2Se_4 and (c) MnSb_2Te_4 along the Γ -Z direction. (d) WCCs Evolution of FM MnSb_2Te_4 . (e) Band structure of FM MnBi_2Se_4 at $\lambda_{\text{soc}} = 1.1$. (f) Energy dispersion of FM MnSb_2Te_4 in the k_x - k_z plane. W and W' indicate the two Weyl points. (g) Fermi arc of FM MnSb_2Te_4 in the (101) surface.

computational details. The lattice constants c (see Table I) used by Zhou group¹⁹ and us are 41.062 and 40.510 Å, respectively, compared with the experimental data of 40.8497 and 40.606 Å obtained from XRD and PND techniques¹⁸, respectively. However, Zhou group¹⁹ reported that FM MnSb_2Te_4 is a type-I Weyl semimetal under small compressive strains or larger SOC strengths. This is in agreement with our calculations. To clarify whether FM MnSb_2Te_4 is a Weyl semimetal or not, intensive and delicate experiments are required. Fig. 4 (f) demonstrates the calculated Fermi arc on the (101) surface of FM MnSb_2Te_4 , which is the fingerprint of Weyl semimetals.

Different from FM MnBi_2Te_4 and MnSb_2Te_4 , which are Weyl semimetals, FM MnBi_2Se_4 is an insulator as Fig. 4 (b) shows. However, linear band crossings or Weyl fermions can be obtained by tuning the SOC strength λ_{soc} larger. Fig. 4 (g) illustrates the band structure of

FM MnBi₂Se₄ along the Γ -Z line at $\lambda_{\text{soc}} = 1.1$, where a Weyl point is clearly seen. Increasing λ_{soc} from 1.1 to 1.3, the material remains in the Weyl state. Besides, a 1% compressive strain also turns FM MnBi₂Se₄ into a type-I Weyl semimetal. The topological phase of FM MnBi₂Se₄ is different from the calculations of Chowdhury *et al.*¹⁷, who have predicted it as a Weyl semimetal at equilibrium lattice constants. Moreover, from the figures in that Ref¹⁷, it is a type-I Weyl semimetal. This agrees with our calculations. It implies that the difference comes from the differences of the optimized lattice constants. As stated before, topological materials usually have very small energy gaps, thus their topological phases are sensitive to lattice constants or experimental conditions. Currently, the experiments on MnBi₂Se₄ are quite limited²⁶, making the judgement on its topological phase unavailable.

C. MnBi₂Te₄, MnBi₂Se₄ and MnSb₂Te₄ slabs

The MnBi₂Te₄ family materials are vdW-layered. They can be mechanically exfoliated into thin flakes from the vdW gaps^{2-4,31}. The obtained flakes or slabs possess intrinsically magnetic order. According to theoretical studies⁷, the FM exchange interaction between the first nearest neighbors ($J_{01} = 0.08 \text{ meV}/\mu_B^2$) strongly dominates over the others in the MnBi₂Te₄ SL, so the SL exhibits a FM ground state; while the inter-layer coupling is AFM. The intrinsically magnetic order breaks the time-reversal symmetry of the slabs and gaps their surface states, and the half-quantum Hall effect can be expected⁸. The spin-up and spin-down surfaces give rise to Hall conductances $\sigma_{xy} = +e^2/2h$ and $-e^2/2h$, respectively. In the AFM slabs of even SLs, the conductances of different surfaces are cancelled, generating axion insulators. The AFM slabs of odd SLs and FM slabs lead to a total Hall conductance $\sigma_{xy} = e^2/h$, corresponding to QAH insulators with non-zero Chern numbers. The QAH conductance σ_{xy} can also be calculated according the Chern number C as³²

$$\sigma_{xy} = \frac{e^2}{2\pi h} \int dk_x dk_y b_z(\mathbf{k}) = \frac{e^2}{h} C. \quad (2)$$

Here $b_z(\mathbf{k})$ is the z component the Berry curvature

$$b(\mathbf{k}) = -\text{Im}\langle \partial_k u(\mathbf{k}) | \times | \partial_k u(\mathbf{k}) \rangle, \quad (3)$$

and $u(\mathbf{k})$ is the periodic part of the Bloch function.

Figure 5 shows the calculated energy band structures of the AFM slabs consisting of 3 and 5 SLs of the three materials, where the Chern numbers are indicated. From Figs. 5 (a) and

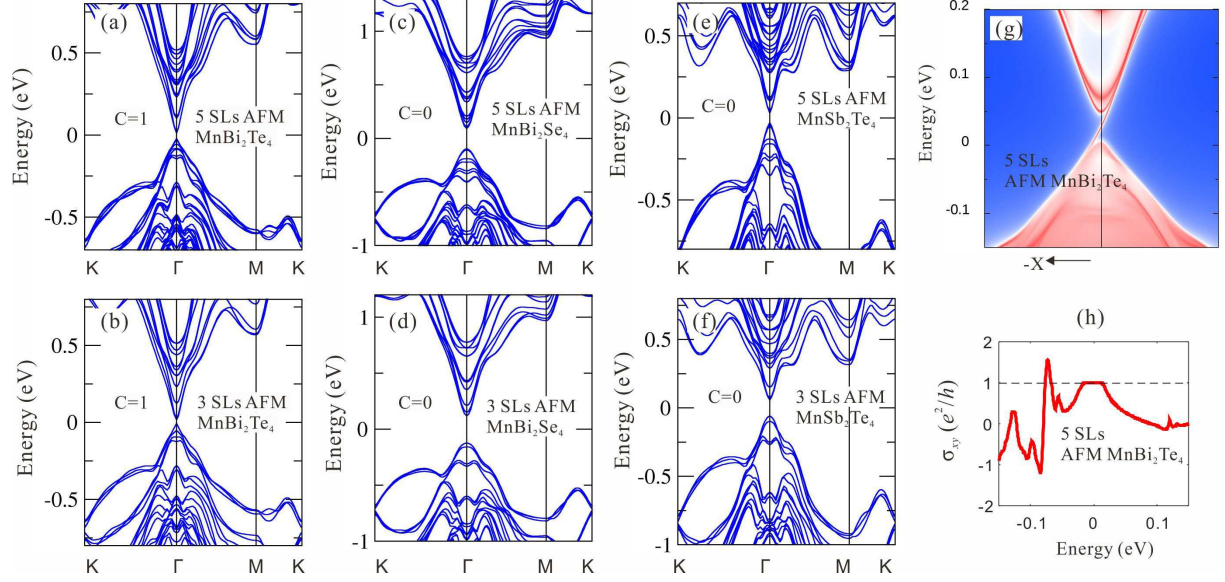


FIG. 5. (a)-(f) Calculated energy band structures of the AFM MnBi_2Te_4 , MnBi_2Se_4 and MnSb_2Te_4 slabs of 3 and 5 SLs, where the Chern numbers are indicated. Calculated (g) chiral edge states and (h) Hall conductance of the AFM MnBi_2Te_4 slab of 5 SLs.

(b) the AFM MnBi_2Te_4 slabs are Chern insulators with $C = 1$, in agreement with previous reports^{7,16}. The energy gaps are 24 and 33 meV at 3 and 5 SLs, respectively, compared with the previously calculated values of 66 and 77 meV⁷, respectively. Larger gaps can be expected for thicker films. According to the picture discussed above, these AFM MnBi_2Te_4 slabs support chiral edge states and give rise to the QAH effect. The calculated band structure of the AFM MnBi_2Te_4 ribbon of 5 SLs is illustrated in Fig. 5 (g) as an example, where the chiral edge state is obvious. Tuning the Fermi level into the energy gap, each edge state contributes a Hall conductance $\sigma_{xy} = e^2/h$ in the absence of the external magnetic field. This is the QAH effect, which has potential applications in dissipationless transportation and topological quantum computation¹. Fig. 5 (h) demonstrates the calculated QAH conductance of the 5 SLs slab. In the energy gap region, the conductance σ_{xy} is exactly quantized to e^2/h . On the contrary, the AFM MnBi_2Te_4 slab of 4 SLs has a Chern number $C = 0$, and the calculated σ_{xy} is zero in the gap region, also in agreement with previous studies⁷. Very recently, the QAH effect has been experimentally observed in the MnBi_2Te_4 films^{2,4}, and the Chern insulator-axion insulator phase transition has also been reported⁴. These observations are consistent with our calculations.

Figures 5 (c) to (f) show that the AFM MnBi_2Se_4 and MnSb_2Te_4 slabs are trivial insula-

tors with the Chern number $C = 0$. This is reasonable. The 3D bulk of AFM MnBi_2Se_4 is a trivial insulator without band inversion. When exfoliated into AFM slabs band inversion cannot be expected too, so the films remain trivial. The 3D bulk of AFM MnSb_2Te_4 is an AFM TI with band inversion, but its energy gap is too small, only 16 meV. To realized band inversion in the AFM MnSb_2Te_4 slabs, the films should be thick enough so that the electronic properties of the films and the bulk converge. Hence, both the AFM MnBi_2Se_4 and the MnSb_2Te_4 slabs are not suitable for observing the QAH effect.

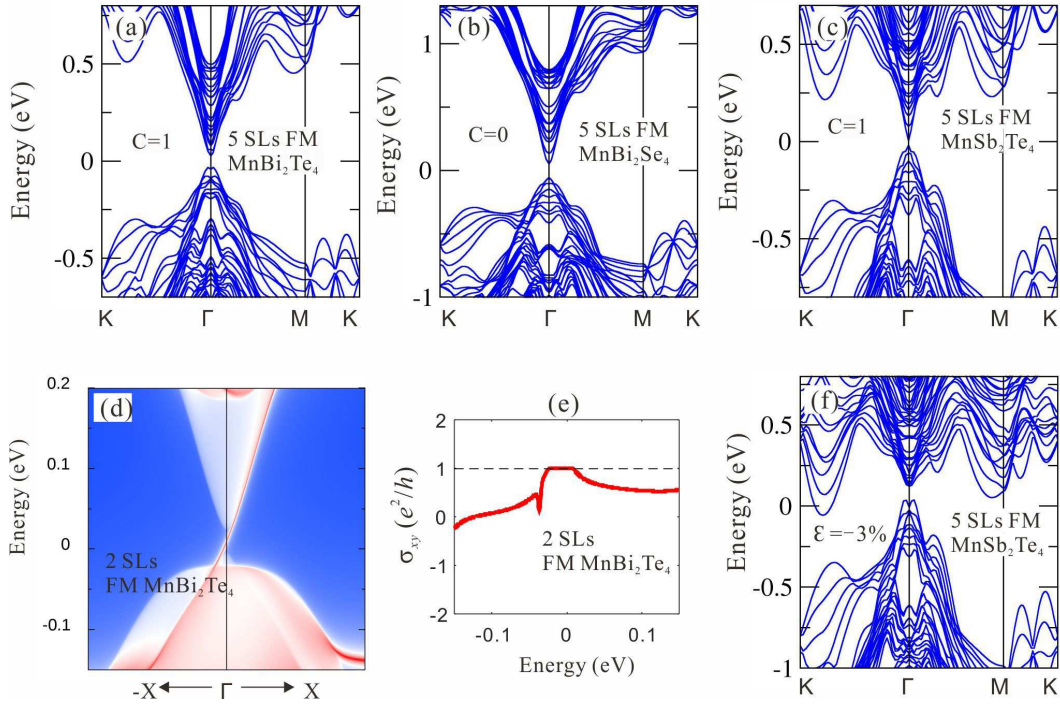


FIG. 6. Calculated energy band structures of the FM (a) MnBi_2Te_4 , (b) MnBi_2Se_4 and (c) MnSb_2Te_4 slabs of 5 SLs, where the Chern numbers are indicated. Calculated (d) chiral edge states and (e) Hall conductance of the FM MnBi_2Te_4 slab of 2 SLs. (f) Band structure of the FM MnSb_2Te_4 slab of 5 SLs at $\epsilon = -3\%$.

The energy band structures and the topological phases of the FM slabs of these materials are also investigated. At equilibrium lattice constants, the FM slabs have direct energy gaps at the Γ point. The FM MnBi_2Te_4 slabs thicker than 2 SLs and the MnSb_2Te_4 slabs thicker than 5 SLs behave as Chern insulators with $C = 1$, while FM MnBi_2Se_4 slabs are always trivial insulators with $C = 0$ irrespective of the film thickness. The energy gaps of the FM MnBi_2Te_4 slabs of 2 to 6 SLs vary from 56 to 72 meV, while the FM MnSb_2Te_4 slabs of

5 and 6 SLs have gaps of 23 and 41 meV, respectively. The band structures of the FM slabs of 5 SLs are shown in Figs. 6 (a) to (c) as examples. The calculated chiral edge states and the conductivity of the FM MnBi_2Te_4 slab of 2 SLs are exhibited in Figs. 6 (d) and (e), respectively. The chiral edge state is obvious, and in the energy gap region the QAH conductivity is quantized to $\sigma_{xy} = e^2/h$. Compared with previous studies, Otrokov *et al.*⁷ have reported that the FM MnBi_2Te_4 slab of 2 SLs is a QAH insulator, in agreement with our calculations. Another interesting study theoretically turned the MnBi_2Te_4 slab of even SLs (4 SLs) from the AFM order to the FM order in a sandwiched $\text{CrI}_3/\text{MnBi}_2\text{Te}_4/\text{CrI}_4$ heterostructure, where the QAH effect was predicted¹⁶.

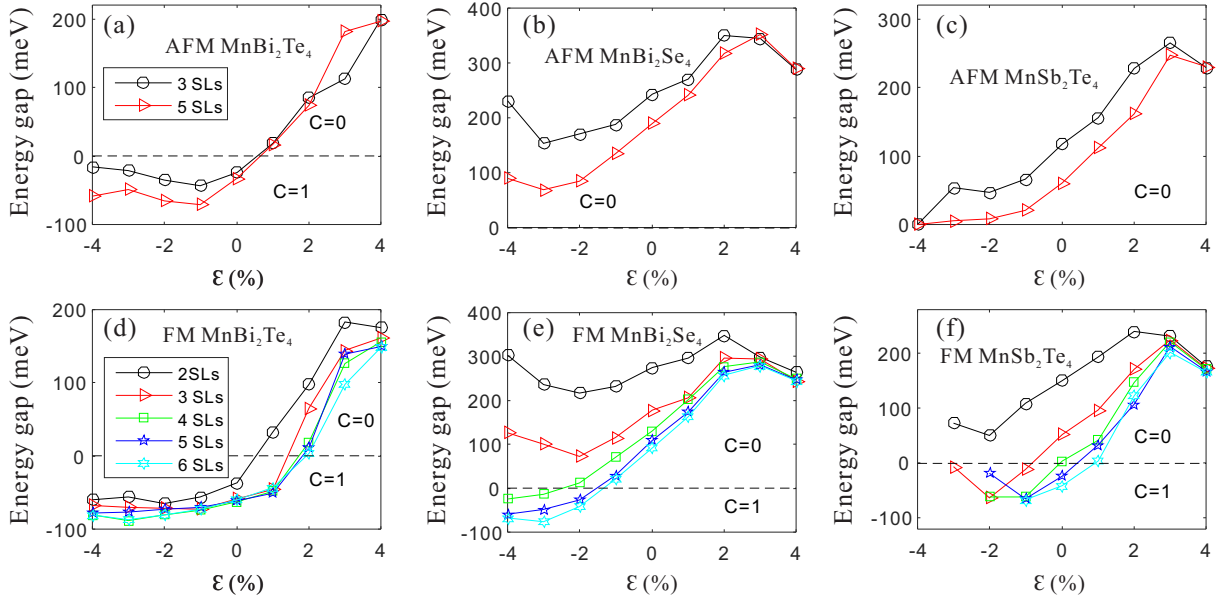


FIG. 7. Energy gaps and topological phases of (a)-(c) AFM and (d)-(f) FM MnBi_2Te_4 , MnBi_2Se_4 and MnSb_2Te_4 slabs at different strains and varying film thicknesses. The legend in (a) applies to (a), (b) and (c), while that in (d) applies to (d), (e) and (f). Positive and negative energy gaps mean that the slabs are trivial insulators with $C = 0$ and Chern insulators with $C = 1$, respectively, and the absolute values of the gaps correspond to the gap sizes.

Figure 7 shows the energy gaps as well as the topological phases of various AFM and FM slabs at isotropic in-plane strains. All the single layers are trivial insulators with energy gaps of several hundreds of meV. Their behaviours under strains are not shown here because topological phase transitions are hard to be achieved using this method. Thicker slabs behave very differently under in-plane strains. The AFM MnBi_2Te_4 slabs of 3 and 5 SLs and the

FM MnBi_2Te_4 slabs thicker than 2 SLs are QAH insulators at equilibrium lattice constants with energy gaps ranging from about 20 to 60 meV. Within $-4\% \leq \epsilon \leq 0$, these slabs keep in the nontrivial state and their energy gaps can be remarkably increased by several tens of meV by in-plane compression. On the other hand, tensile strains from 1% to 2% are able to turn the slabs into trivial insulators.

Both the AFM and the FM MnBi_2Se_4 slabs of 2 SLs or thicker are trivial insulators at $\epsilon = 0$. Topological phase transitions from trivial insulators to Chern insulators can be induced in the FM MnBi_2Se_4 slabs thicker than 4 SLs by applying compressive strains larger than 2% or 3%. The AFM and the thinner FM MnBi_2Se_4 slabs remain trivial when changing ϵ from -4% to 4% . The electronic behaviours of the AFM MnSb_2Te_4 slabs are similar to those of the AFM MnBi_2Se_4 slabs. At equilibrium lattice constants, the AFM MnSb_2Te_4 slabs of 3 and 5 SLs are trivial, and small or moderate strains cannot result in topological phase transitions. The FM MnSb_2Te_4 slabs of 5 and 6 SLs are Chern insulators with $C = 1$, and thinner films are trivial insulators. However, these trivial FM slabs can also be turned into Chern insulators by 1% to 2% in-plane compression except the 1 SL slab. It should be noted that in Fig. 7 (f) only the energy gaps and topological phases for $\epsilon \geq -2\%$ or $\epsilon \geq -3\%$ are shown. This is because under larger compressive strains, the CBM becomes lower than the VBM, making the slabs metallic. We show the band structure of the 5 SLs FM MnSb_2Te_4 slab under $\epsilon = -3\%$ in Fig. 6 (f), which can help us to understand the electronic behaviours of the FM MnSb_2Te_4 slabs under large compressive strains.

IV. DISCUSSION

This work provides not only consistent results with previous theoretical studies and experimental observations but also new findings. Both this work and previous studies^{3,5,6} agree that the MnBi_2Te_4 bulk is an AFM TI, while in the FM order it is a Weyl semimetal. In experiment, the energy gap has been observed on the (001) surface of MnBi_2Te_4 ³, and the QAH effect has been realized in a MnBi_2Te_4 slab of 5 SLs at 1.4 K². Though the MnBi_2Te_4 slabs have a AFM ground state, studies on their FM phase is also of interest because their magnetic order is artificially controllable. One experimental example is that the axion insulator to Chern insulator phase transition has been achieved in the MnBi_2Te_4 slabs of 6 SLs by a moderate magnetic field⁴; while an theoretical example is that the MnBi_2Te_4 slab

of even SLs (4 SLs) can be turned from the AFM order to the FM order in a sandwiched $\text{CrI}_3/\text{MnBi}_2\text{Te}_4/\text{CrI}_3$ heterostructure¹⁶. The obtained FM slabs are found to support the QAH effect, also in agreement with our calculations that the FM MnBi_2Te_4 slabs thicker than 2 SLs are Chern insulators. In addition, the calculated topological nature of both the AFM and the FM MnBi_2Te_4 slabs of different SLs also agrees with previous theoretical studies^{7,16}. A recent study³³ has predicted the high-Chern-number Chern insulators in MnBi_2Te_4 slabs thicker than 8 SLs. The prediction is interesting, and investigations on thicker MnBi_2Te_4 slabs remain essential.

It seems that the topological phases of the MnSb_2Te_4 bulk in our work differ from the reports of Zhou *et al.*¹⁹, but in fact they are not contradictory. Zhou *et al.* performed calculations based on the experimental lattice constants and the Wyckoff atomic positions, where the Mn and Sb atoms are mixed, while we calculate a perfect MnSb_2Te_4 crystal at the theoretical lattice constants without any atomic mixing. Therefore, the differences can be explained and understood. Murakami *et al.*¹⁸ calculated the properties of MnSb_2Te_4 and predicted a Weyl semimetal, in agreement with our results. The differences of the topological nature of MnBi_2Se_4 between our results and the calculations of Chowdhury *et al.*¹⁷ can also be attributed to the atomic-structure differences. Careful experimental studies are needed to clarify the topological properties of MnBi_2Se_4 and MnSb_2Te_4 .

The topological phases of the considered slabs are sensitive to strains, but as far as we are aware such investigations are currently unavailable. According to our calculations, small isotropic in-plane compressive strains remarkably increase the nontrivial energy gaps of Chern insulators, or change some trivial slabs into QAH insulators. On the contrary, small isotropic in-plane tensile strains around 1% turn the films from the nontrivial phase to the trivial phase. For the realization and observation of the QAH effect, the MnBi_2Te_4 slabs are ideal, while the MnBi_2Se_4 and MnSb_2Te_4 films are not. On the other hand, the in-plane compressive strains are suggested, while the out-of-plane compressive strains are not recommended. With a common positive Poisson's ratio, the compression of the out-of-plane lattice constant c usually leads to the dilation of the in-plane constant a . Our calculations have confirmed this, finding that such operations are adverse to obtain QAH insulators in the present materials.

V. CONCLUSION

The electronic structures and topological phases of magnetic layered materials MnBi_2Te_4 , MnBi_2Se_4 and MnSb_2Te_4 are systematically investigated. According to first-principles calculations, these compounds energetically prefer the AFM state. MnBi_2Te_4 and MnSb_2Te_4 are AFM TIs in the AFM state, which become Weyl semimetals in the FM state. MnBi_2Se_4 is trivially insulating in both AFM and FM states, but it can be turned into an AFM TI or a Weyl semimetal by increasing the SOC strength or applying compressive strains. Under equilibrium lattice constants, the FM MnBi_2Te_4 slabs thicker than 2 SLs and the AFM MnBi_2Te_4 slabs thicker than 3 SLs are Chern insulators. The AFM MnBi_2Se_4 and the MnSb_2Te_4 slabs are trivial insulators, and they are hard to be turned into Chern insulators by applied strains. The FM MnSb_2Te_4 slabs thicker than 5 SLs are Chern insulators, while the FM MnBi_2Se_4 slabs are trivial. Some trivial FM slabs can be turned into Chern insulators through small or moderate compressive strains, and some Chern insulating slabs can be easily turned into trivial insulators by 1% to 2% tensile strains. The topological phases of MnBi_2Te_4 have been experimentally confirmed, while those of MnBi_2Se_4 and MnSb_2Te_4 have not. In certain cases our calculations give different results from previous calculations, thus they call for careful experimental studies on MnBi_2Se_4 and MnSb_2Te_4 . The electronic behaviours of the bulks and slabs of all three materials under applied strains and varying film thicknesses are summarized in Fig. 3 (a) and Fig. 7. The present work provides references for the experimental control of the topological phases of the MnBi_2Te_4 family materials, especially for the experimental realization of the QAH effect.

ACKNOWLEDGEMENT

P. Li would like to thank L. Zhou and J. Li for helpful discussions. This work is supported by the National Natural Science Foundation of China (Grant Nos. U1632272 and 11521404), the Natural Science Foundation of Anhui Province (Grant No. 1308085QA05), and the Research Foundation of Anhui Jianzhu University (Grant Nos. 2017QD19 and 2018QD11).

* liping@ahjzu.edu.cn

[†] wdluo@sjtu.edu.cn

- ¹ Y. Tokura, K. Yasuda, and A. Tsukazaki, *Nat. Rev. Phys.* **1**, 126 (2019).
- ² Y. Deng, Y. Yu, M. Z. Shi, Z. Guo, Z. Xu, J. Wang, X. H. Chen, and Y. Zhang, *Science* **367**, 895 (2020).
- ³ M. M. Otrokov, I. I. Klimovskikh, H. Bentmann, D. Estyunin, A. Zeugner, Z. S. Aliev, S. Gaß, A. U. B. Wolter, A. V. Koroleva, A. M. Shikin, M. Blanco-Rey, M. Hoffmann, I. P. Rusinov, A. Y. Vyazovskaya, S. V. Eremeev, Y. M. Koroteev, V. M. Kuznetsov, F. Freyse, J. Sanchez-Barriga, I. R. Amiraslanov, M. B. Babanly, N. T. Mamedov, N. A. Abdullayev, V. N. Zverev, A. Alfonsov, V. Kataev, B. Buchner, E. F. Schwier, S. Kumar, A. Kimura, L. Petaccia, G. D. Santo, R. C. Vidal, S. Schatz, K. Kißner, M. Unzelmann, C. H. Min, S. Moser, T. R. F. Peixoto, F. Reinert, A. Ernst, P. M. Echenique, A. Isaeva, and E. V. Cholkov, *Nature* **576**, 416 (2019).
- ⁴ C. Liu, Y. Wang, H. Li, Y. Wu, Y. Li, J. Li, K. He, Y. Xu, J. Zhang, and Y. Wang, *Nat. Mater.* **19**, 522 (2020).
- ⁵ D. Zhang, M. Shi, T. Zhu, D. Xing, H. Zhang, and J. Wang, *Phys. Rev. Lett.* **122**, 206401 (2019).
- ⁶ J. Li, Y. Li, S. Du, Z. Wang, B.-L. Gu, S.-C. Zhang, K. He, W. Duan, and Y. Xu, *Sci. Adv.* **5**, eaaw5685 (2019).
- ⁷ M. M. Otrokov, I. P. Rusinov, M. Blanco-Rey, M. Hoffmann, A. Y. Vyazovskaya, S. V. Eremeev, A. Ernst, P. M. Echenique, A. Arnau, and E. V. Cholkov, *Phys. Rev. Lett.* **122**, 107020 (2019).
- ⁸ R. S. K. Mong, A. M. Essin, and J. E. Moore, *Phys. Rev. B* **81**, 245209 (2010).
- ⁹ C.-Z. Chang, J. Zhang, X. Feng, J. Shen, Z. Zhang, M. Guo, K. Li, Y. Ou, P. Wei, L.-L. Wang, Z.-Q. Ji, Y. Feng, S. Ji, X. Chen, J. Jia, X. Dai, Z. Fang, S.-C. Zhang, K. He, Y. Wang, L. Lu, X.-C. Ma, and Q.-K. Xue, *Science* **340**, 167 (2013).
- ¹⁰ R. Yu, W. Zhang, H.-J. Zhang, S.-C. Zhang, X. Dai, and Z. Fang, *Science* **329**, 61 (2010).
- ¹¹ Y. L. Chen, J.-H. Chu, J. G. Analytis, Z. K. Liu, K. Igarashi, H.-H. Kuo, X. L. Qi, S. K. Mo, R. G. Moore, D. H. Lu, M. Mashimoto, T. Sasagawa, S. C. Zhang, I. R. Fisher, Z. Hussain, and Z. X. Shen, *Science* **329**, 659 (2010).
- ¹² F. Katmis, V. Lauter, F. S. Nogueira, B. H. Assaf, M. E. Jamer, P. Wei, B. Satpati, J. W. Freeland, I. Eremin, D. Heiman, P. Jarillo-Herrero, and J. S. Moodera, *Nature* **533**, 513 (2016).
- ¹³ W. Luo and X.-L. Qi, *Phys. Rev. B* **87**, 085431 (2013).
- ¹⁴ P. Li, J. Yu, J. Xu, L. Zhang, and K. Huang, *Physica B* **573**, 77 (2019).

- ¹⁵ Y. Peng and Y. Xu, Phys. Rev. B **99**, 195431 (2019).
- ¹⁶ H. Fu, C.-X. Liu, and B. Yan, Sci. Adv. **6**, eaaz0948 (2020).
- ¹⁷ S. Chowdhury, K. F. Garrity, and F. Tavazza, npj Comput. Mater. **5**, 33 (2019).
- ¹⁸ T. Murakami, Y. Nambu, T. Koretsune, G. Xiangyu, T. Yamamoto, C. M. Brown, and H. Kageyama, Phys. Rev. B **100**, 195103 (2019).
- ¹⁹ L. Zhou, Z. Tan, D. Yan, Z. Fang, Y. Shi, and H. Weng, Phys. Rev. B **102**, 085114 (2020).
- ²⁰ G. Kresse and Furthmüller, Phys. Rev. B **54**, 11169 (1996).
- ²¹ J. P. Perdew, K. Burke, and M. Ernzerhof, Phys. Rev. Lett. **77**, 3865 (1996).
- ²² J. Klimeš, D. R. Bowler, and A. Michaelides, J. Phys.: Condens. Matter **22**, 022201 (2010).
- ²³ J. Heyd, G. Scuseria, and M. Ernzerhof, J. Chem. Phys. **118**, 8207 (2003).
- ²⁴ J. Heyd, G. Scuseria, and M. Ernzerhof, J. Chem. Phys. **124**, 219906 (2006).
- ²⁵ Q. Wu, S. Zhang, H.-F. Song, M. Troyer, and A. A. Soluyanov, Comput. Phys. Commun. **224**, 405 (2018).
- ²⁶ C. Nowka, M. Gellesch, J. E. H. Borrero, S. Partzsch, C. Wuttke, F. Steckel, C. Hess, A. U. B. Wolter, L. T. C. Bohorquez, B. Büchner, and S. Hampel, J. Cryst. Growth **459**, 81 (2017).
- ²⁷ P. Li, J. Yu, J. Xu, L. Zhang, and K. Huang, Adv. Quantum Technol. **2**, 201900033 (2019).
- ²⁸ P. Li and W. Luo, Sci. Rep. **6**, 25423 (2016).
- ²⁹ M. Z. Hasan and C. L. Kane, Rev. Mod. Phys. **82**, 3045 (2010).
- ³⁰ X.-L. Qi and S.-C. Zhang, Rev. Mod. Phys. **83**, 1057 (2011).
- ³¹ G. Shi, M. Zhang, D. Yan, H. Feng, M. Yang, Y. Shi, and Y. Li, Chin. Phys. Lett. **37**, 047301 (2020).
- ³² L. Šmejkal, Y. Mokrousov, B. Yan, and A. H. MacDonald, Nat. Phys. **14**, 242 (2018).
- ³³ J. Ge, Y. Liu, J. Li, H. Li, T. Luo, Y. Wu, Y. Xu, and J. Wang, Natl. Sci. Rev. **7**, 1280 (2020).